

Haverford College

Haverford Scholarship

Faculty Publications

Physics

2015

An improved method for object detection in astronomical images

Caixia Zheng

Jesus Pulido

Paul Thorman

Haverford College, pthorman@haverford.edu

Follow this and additional works at: https://scholarship.haverford.edu/physics_facpubs

Repository Citation

Zheng, C. X.; Pulido, J.; Thorman, P.; Hamann, B. "An improved method for object detection in astronomical images," MNRAS 451 (4):4445-4459. 2015.

This Journal Article is brought to you for free and open access by the Physics at Haverford Scholarship. It has been accepted for inclusion in Faculty Publications by an authorized administrator of Haverford Scholarship. For more information, please contact nmedeiro@haverford.edu.

An improved method for object detection in astronomical images

Caixia Zheng,^{1,2★} Jesus Pulido,^{3★} Paul Thorman^{4,5★} and Bernd Hamann³

¹*School of Computer Science and Information Technology, Northeast Normal University, Changchun 130117, China*

²*School of Mathematics and Statistics, Northeast Normal University, Changchun 130024, China*

³*Institute for Data Analysis and Visualization, Department of Computer Science, University of California, Davis, One Shields Avenue, Davis, CA 95616, USA*

⁴*Department of Physics, Haverford College, 370 Lancaster Avenue, Haverford, PA 19041, USA*

⁵*Department of Physics, University of California, Davis, One Shields Ave, Davis, CA 95616, USA*

Accepted 2015 June 1. Received 2015 May 30; in original form 2015 January 14

ABSTRACT

This paper introduces an improved method for detecting objects of interest (galaxies and stars) in astronomical images. After applying a global detection scheme, further refinement is applied by dividing the entire image into several irregularly sized sub-regions using the watershed segmentation method. A more refined detection procedure is performed in each sub-region by applying adaptive noise reduction and a layered strategy to detect bright objects and faint objects, respectively. Finally, a multi-threshold technique is used to separate blended objects. On simulated data, this method can detect more real objects than SExtractor at comparable object counts (91 per cent versus 83 per cent true detections) and has an increased chance of successfully detecting very faint objects, up to 2 mag fainter than SExtractor on similar data. Our method has also been applied to real observational image data sets to verify its effectiveness.

Key words: methods: data analysis – techniques: image processing – astrometry.

1. INTRODUCTION

Astronomical images provide useful information about the physical characteristics and evolution of celestial objects in the Universe. In order to better understand the cosmos, astronomers have to search for astronomical objects (sources) in extremely high resolution images captured. However, due to the vast number of objects (dozens per square arcminute, in deep surveys) in astronomical images, many of which overlap and are very faint, it becomes overwhelming for a user to manually identify such objects. For this reason, it is necessary to develop efficient and robust algorithms to automatically detect the objects in astronomical images by using highly specialized and adapted image processing and computer vision techniques. Compared to ordinary images, astronomical images have a higher proportion of noise relative to the signals of interest, a larger dynamic range of intensities, and objects with unclear boundaries. These characteristics make detection of astronomical objects extremely challenging and complicated.

Several approaches have been proposed to perform object detection in astronomical images. Slezak, Bijaoui & Mars (1988) applied ellipse fitting and radial profile determination to automatically detect objects in images. In this method, Gaussian fitting of histograms was used for noise characterization, and detection

thresholds were determined based on the peaks of the distribution. Damiani et al. (1997) used Gaussian fitting, a median filter, and the ‘Mexican hat’ wavelet transform to smooth the fluctuations in the background of the image, and objects were detected as the local peaks whose pixel values exceeded some thresholds. Andreon et al. (2000) classified objects and background by using principal component analysis (PCA) neural networks. Perret, Lefevre & Collet (2008) proposed a morphological operator called hit-or-miss transform to enhance objects for better detection. Guglielmetti, Fischer & Dose (2009) adapted Bayesian techniques to detect objects based on prior knowledge. The inverse-Gamma function and exponential were used as the probability density functions and thin plate splines were used to represent the background. Broos et al. (2010) developed a wavelet-based strategy to reconstruct images, and defined the peaks of reconstructed images as the objects. Bertin & Arnouts (1996) developed the widely used SExtractor software tool based on local background estimation and thresholding to detect objects. Generally, these methods can produce good results but easily miss faint objects or detect a relatively large number of false positives under several image conditions. Low signal-to-noise ratio, variable background, and large differences in brightness between the brightest and faintest objects in the images can lead to these problems.

Recently, there has been a focus on detecting more faint objects in astronomical images. For instance, Torrent et al. (2010) detected faint compact sources by what they called a boosting classifier in radio frequency images. In this approach, a dictionary of possible object classes needs to be built first by cataloguing local features

* E-mail: zhengcx788@163.com (CZ); jpulido@ucdavis.edu (JP); pthorman@haverford.edu (PT)

extracted from images convolved with different filters. Afterwards, the boosting classifier was trained on the training image data set to obtain a near-optimal set of classification parameters for extracting objects in the test data set. The time taken to build the dictionary and train the classifier is significant and it requires an initial set of ground-truth images to be constructed. Peracaula et al. (2009, 2010) used a local peak search based on wavelet decomposition and contrast radial functions to detect faint compact sources in radio and infrared images. In addition, Masias et al. (2012) found that multi-scale transforms such as wavelet decomposition are commonly applied to infrared, radio, and X-ray images; however, more basic image transformations (e.g., filters and local morphological operators) perform well when applied to multi-band and optical images.

In this paper, we present a novel object detection method for optical images taken by a wide-field survey telescope by employing irregularly sized sub-regions and a layered detection strategy. Several image pre-processing steps are incorporated to enhance images, including greyscale stretching, background estimation, histogram equalization and adaptive noise reduction based on a noise-level estimation technique. A working prototype of the code is also made available.¹

This paper is structured as follows: Section 2 describes our method. Section 3 evaluates the accuracy of our method for a synthetic simulated data set and an observational data set, comparing the obtained results with those obtained by a competing method. Section 4 provides conclusions and points out possible directions for future work.

2. METHOD

2.1 Overview

The simultaneous detection of both bright and faint objects in astronomical images with many objects of varying sizes and brightness is challenging. We present a local and layered detection scheme which, based on the appropriate image transformations and adaptive noise removal, deals with bright and faint objects separately. The fundamental idea and goal of our approach is to extract more real objects and more faint objects close to bright objects in images with very large dynamic intensity ranges and high levels of noise. To illustrate this, the results of applying both our method and `SEXTRACTOR` to the same region of LSST's publicly available image simulations are shown in Fig. 1. The images in Fig. 1(a) show the same region in which many faint objects are present. In this region, more genuine faint objects (marked by triangles) were detected by our method. The images in Fig. 1(b) show a region that has a high dynamic range, including a bright object and some faint objects. More authentic faint objects (marked by triangles) in the neighbourhood of the bright one are detected by our method.

Our method can be understood as consisting of two main components: global detection (which can be run as an independent detection routine) and local detection. Global detection includes several simple steps for fast detection of objects for an entire image. The global method adopts smoothing based on a Gaussian filter (Blinchikoff & Zverev 2001), background subtraction (Bertin & Arnouts 1996), and histogram equalization of intensities (Laughlin 1981) to remove noise and enhance the image. Objects are detected

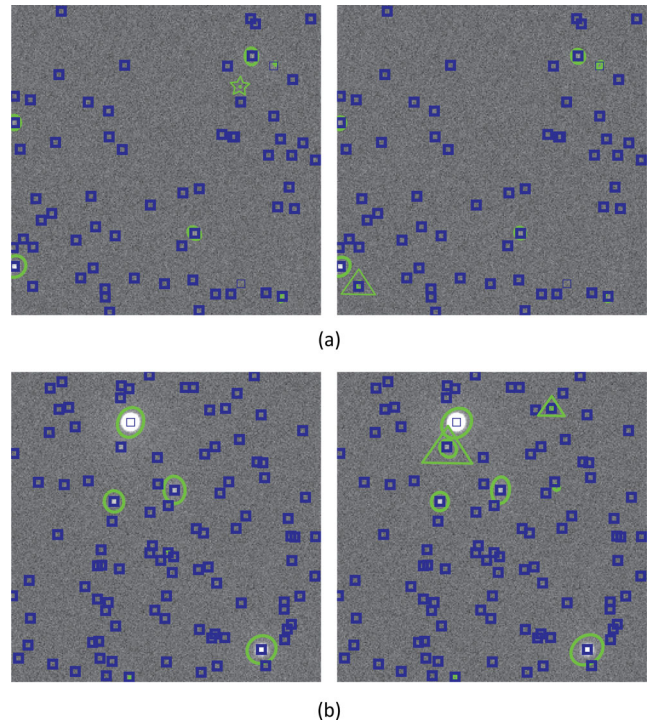


Figure 1. The contribution made in this paper is the presentation of a highly specialized and adapted method to detect (a) more real objects and (b) more faint objects in the neighbourhood of bright ones. Squares mark object positions known to be true. Ellipses on the left-column pictures show objects detected by the competing method (`SEXTRACTOR`); among them there is one false positive (marked by the pentagram). Ellipses on the right-column pictures indicate objects detected by our method, and triangles mark real, faint objects exclusively detected by our method. Comparing the left-column pictures and the right-column pictures, our method detects more real, faint objects with fewer false positives, and it can find more faint objects in the neighbourhood of bright objects.

with Otsu's method (Otsu 1979). When the global method is used alone, deblending is applied as a last step for attempting to separate touching objects that have been detected. The local detection component consists of five major steps: division of the image into irregular sub-regions, image transformation, adaptive noise removal, layered object detection, and separation of touching objects through deblending. Fig. 2 shows a flow chart of the overall procedure of our method, demonstrating the primary steps involved.

2.2 Global detection method

The global detection in our method consists of a Gaussian filter, background subtraction, histogram equalization, and thresholding by Otsu's method. These steps are applied to a normalized image with intensities from 0 to 1. As these steps are prerequisites to the local detection method, these global detection components will be further described alongside the local detection method in the next section.

2.3 Local detection method

Initially, the local method divides an entire image into non-uniform and non-overlapping sub-regions by using the watershed segmentation method (Beucher & Meyer 1993). This method subjects an image a changing threshold that starts at the value of the

¹ <https://github.com/zhengcx789/Object-Detection-in-Astronomical-Images>

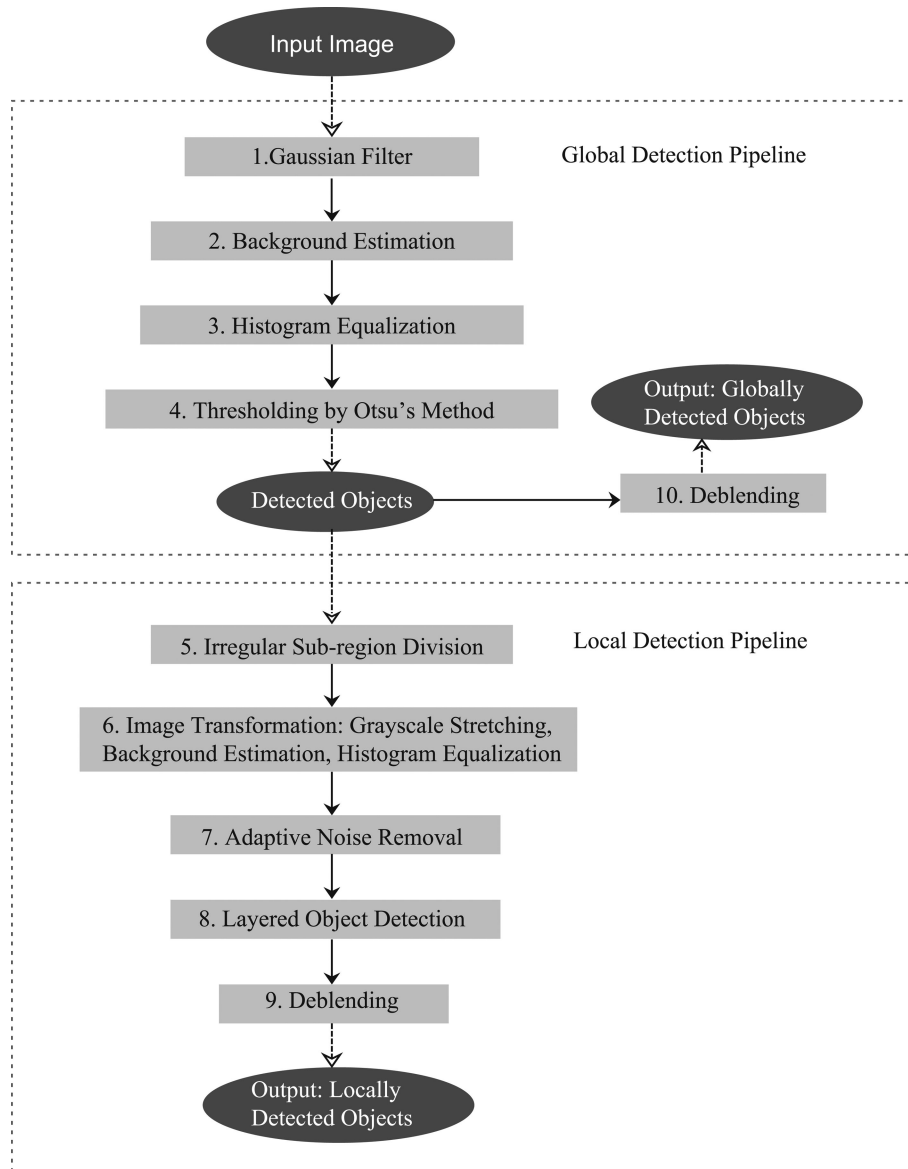


Figure 2. Complete object detection pipeline. Rectangles denote computational processes executed, while ellipses denote data used or created. Specifically, the novel steps used in our method are irregular sub-region division, adaptive noise removal, and layered object detection.

brightest pixels and gradually decreases. At each threshold value, pixels that cross the threshold are assigned to the neighbouring sub-region until the image has been completely segmented. To obtain the best results through the watershed segmentation method, several large and bright objects are extracted by the global detection component as the seed points for generating sub-regions. This division benefits later object detection steps in the pipeline.

The division is followed by the image transformation step, in which we apply grayscale stretching, background estimation, and histogram equalization. This step improves the contrast of images for faint object detection.

Adaptive noise removal is used to suppress undesired noise in astronomical images. The dynamically sized Gaussian filter is created based on the noise-level estimation for more accurate noise reduction.

When the local method performs astronomical object detection and extraction, a layered detection is used to detect bright and faint objects separately. The aim of the layered detection is to weaken

the influence of the large and bright objects on the detection of faint objects.

Finally, the detected objects are individually checked to determine whether deblending is needed through the use of multi-threshold techniques and an additional watershed application.

2.3.1 Irregular sub-region division

In general, astronomical images contain background noise that makes it difficult to apply object detection directly as a global operator. Background noise can vary widely in different regions of an image. The traditional approach to solve this problem is to use a uniform mesh to divide the image into small square or rectangular regions. The background is evaluated and a detection threshold is defined for each region (as done by `SEXTRACTOR`). The choice of mesh size is a key factor in background estimation and threshold computations. If the size is too large, small variations in the background cannot be described. Likewise if too small, the background

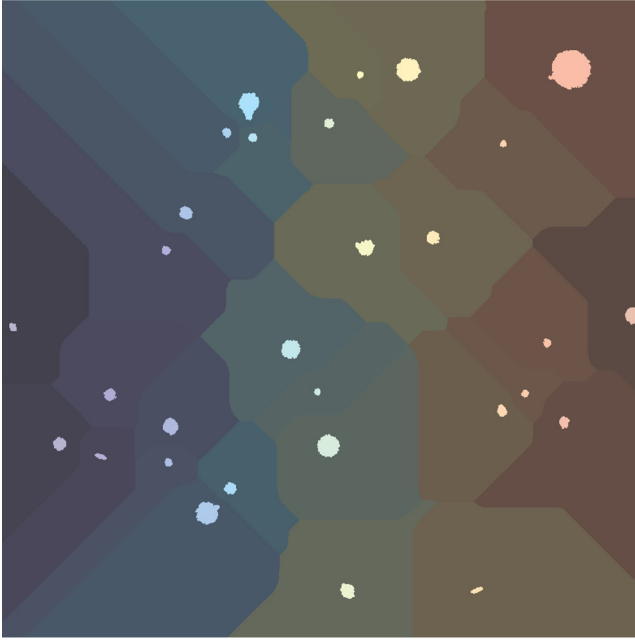


Figure 3. Irregularly sized sub-regions created by the watershed segmentation method. The different colour areas denote sub-regions obtained; the white object in each sub-region is the brightest object, which was used as the seed point.

noise and the presence of real objects will affect the background estimation.

The watershed segmentation method has been broadly used in the fields of computer vision and graphics. Beucher & Meyer (1993) first proposed and applied this method for the segmentation of regions of interest in images. Later, Mangan & Whitaker (1999) found a new application of watersheds to partition 3D surface meshes for improved rendering. Inspired by this approach, we present a novel non-linear partitioning method which divides an image into local regions.

The watershed segmentation method takes every local minimum pixel as a seed point to grow by merging surrounding non-seed pixels for the purpose of image segmentation. In our application, we determine several very bright objects found by global detection as seed points and set the pixel value of these seed points to 0, and all the remaining pixel values in the image are set to 1. The seed points are grown to obtain sub-regions and stop only when neighbouring sub-regions touch each other and cover the entire image. The results of the division can be seen in Fig. 3 where 30 brightest objects are selected as seed points.

This method can assure that each obtained sub-region includes at least one very large and bright object. One advantage of having these sub-regions is that more accurate thresholds can be computed for detecting more real objects. Another advantage over the conventional approach is that the watershed prevents bright objects from being split between neighbouring regions as the method always creates regions around objects. In Fig. 3, the usage of the watershed segmentation method allows for the isolation of the large star that also contains camera artefacts. This region can be handled better for extraction of objects compared to a conventional partitioning scheme where this large star would span multiple regions. Further, by combining this sub-region division with layered detection, more faint objects can be detected.

2.3.2 Image transformation

Astronomical images contain several characteristics that make object detection difficult. These include but are not limited to the high dynamic intensity range and variable background intensity. The proposed image transformation step is carried out to make the objects more visible, remove variable background, and enhance the contrast of image prior to the detection of objects.

Although the original intensity values of an astronomical survey image of an uncrowded field might range from 0 to 10^5 (depending on the gain of the amplifiers and the depth of the CCD wells), most of the pixel values lie within a small intensity range near the median. This makes the visualization of the entire data set containing a full range of intensities difficult (Taylor et al. 2003; Stil et al. 2006). Greyscale stretching is used to stretch the image intensities around an appropriate pixel value to make details more obvious for automatic detection. The greyscale stretching function used in our method is the sigmoid function (Gevrekci & Gunturk 2009), which has the following form:

$$f(I(x, y)) = \frac{1}{1 + e^{-s(I(x, y) - c)}}, \quad (1)$$

where c defines the intensity centre, around which the intensity is stretched, s determines the slope of this function, and $I(x, y)$ is the normalized intensity value of the pixel. In experiments, $I(x, y)$ is computed according to the following formula for making the image intensity range from 0 to 1,

$$I(x, y) = \sqrt{(I_{\text{ori}}(x, y) - I_{\text{min}})/(I_{\text{max}} - I_{\text{min}})}, \quad (2)$$

where $I_{\text{ori}}(x, y)$ is the original image intensity at (x, y) , I_{min} and I_{max} are the minimum and maximum intensities of the image. Due to the large dynamic intensity range of astronomical images, the square root operator is applied to avoid intensities so small as to suffer from numerical noise in floating point operations. Fig. 4 illustrates the different shapes of the sigmoid function with different parameters. In our method, c is the median intensity of the image, and s is set to 40. The result of greyscale stretching is shown in Fig. 5. When comparing Figs 5(a) and (b), more objects can be clearly seen in (b) otherwise not visible in the original image (a). The effectiveness

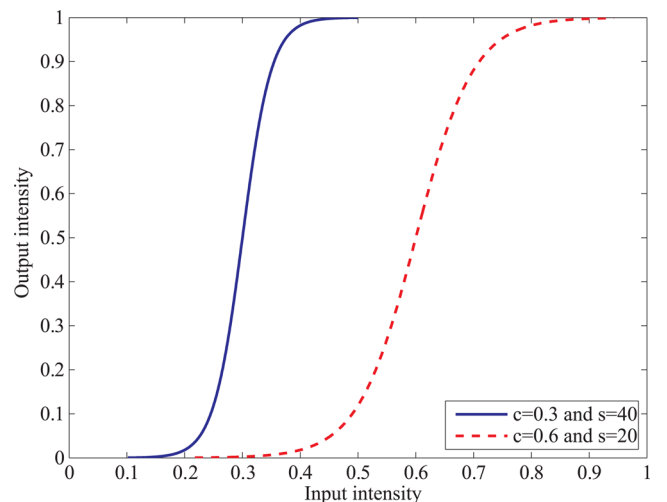


Figure 4. The shape of the sigmoid function. The x -axis is the original intensity of images, and the y -axis is the transformed intensity obtained by using the sigmoid function transformation. With this transformation, the intensity of the high-intensity pixels becomes higher, while that of the low-intensity pixels gets lower.

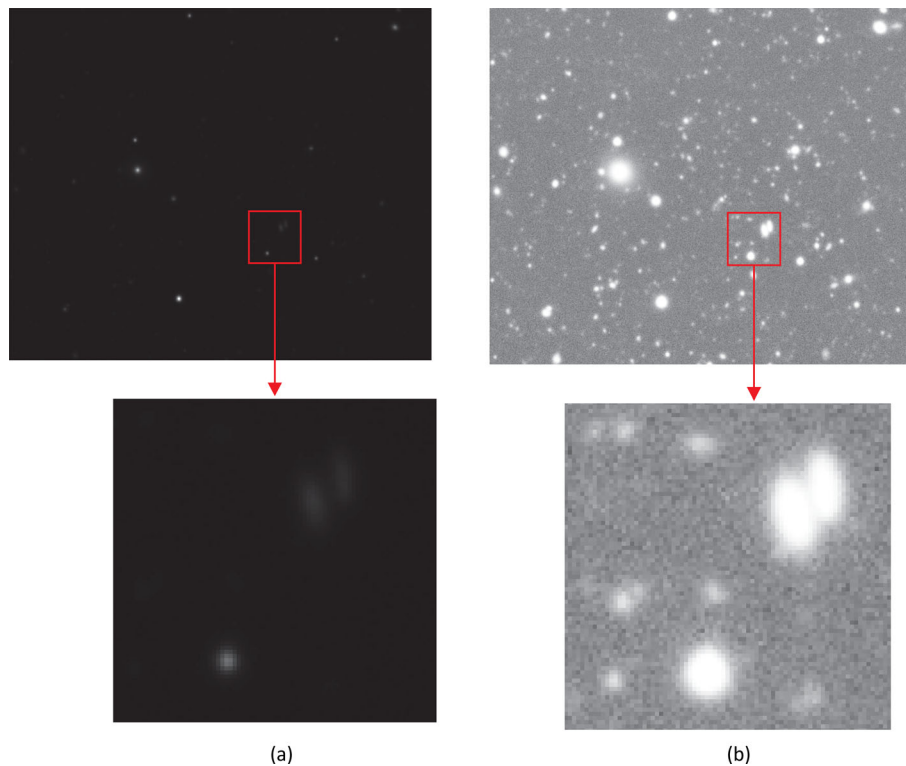


Figure 5. Results of greyscale stretching. The top picture in panel (a) is the original astronomical image, and the bottom picture in panel (a) provides a magnified view of the area in the rectangle. The top picture in panel (b) is the image obtained by greyscale stretching, and the bottom picture in panel (b) provides a magnified view of the area in the rectangle. Comparing panels (a) and (b), the objects in panel (b) are more clearly visible.

of greyscale stretching is apparent for making faint objects more visible which benefits faint object detection.

Besides the high dynamic range, the second factor that needs to be considered is the background noise in astronomical images. Due to this, the background of an image needs to be estimated and subtracted from the original image for improving the object detection quality. This operation is achieved in our pipeline by using an approach applied in SExtractor (Bertin & Arnouts 1996) where the background is computed as a function of the statistics of an image. The value of the background BG in the non-crowded field is estimated as the mean of the clipped histogram of pixel distribution, and in the crowded field, the background BG is computed as

$$BG = 2.5 \cdot \text{med} - 1.5 \cdot m, \quad (3)$$

where ‘med’ is the median and m is the mean of the clipped histogram of pixel distribution.

Astronomical images typically have low image contrast and cause faint objects to blend in with the background. Normally this causes these faint objects to be classified as the background and ignored when object detection is done. The peak distribution of the intensity histogram of astronomical images is typically concentrated in the lower spectrum. Since fainter objects are generally more common than brighter ones, many pixels will appear empty and contain no detectable objects at all. Histogram equalization is used in our pipeline to further enhance the quality of the image by scaling the intensities to effectively spread out the most frequent values to generate a better distribution compared to the original intensity histogram. This non-linear operation is only applied for the purpose of object detection and not used for the purpose of computing photometry. This procedure strengthens the contrast of the objects against the background making the boundaries of objects clearer and

easier to identify. It can result in a substantial improvement to the quality of the final detection. The result of histogram equalization is given in Fig. 6. Compared to the image in Fig. 5(b), the object intensities are strengthened and the boundaries are clearer.

2.3.3 Adaptive noise removal

The ability to detect objects is commonly limited at the faintest flux levels by the background noise, otherwise known as the apparent brightness of objects. In modern charge-coupled devices (CCDs), apparent brightness is dominated by photon shot noise on the diffuse emission from the Earth’s atmosphere. Some improvement in object detection can be achieved simply through filtering of the image for noise reduction prior to detection. A spatial Gaussian filter is used in our method as a simple and effective noise reduction method. As mentioned in Masias et al. (2012) and Stetson (1987), Gaussian filter can also be seen as an approximation to the point spread function, which would act as a signal-matched filter to enhance the real objects.

The noise levels within astronomical images vary; for instance, the neighbourhood of a large, bright object (which might also be the source of image artefacts) has high noise levels. An adaptive noise removal strategy is carried out in our method based on the estimation of noise levels. Before applying the Gaussian filter, the noise level in each local sub-region is estimated by the algorithm proposed by Liu, Tanaka & Okutomi (2012). This method uses numerous image regions and selects the patches with the maximum eigenvalue of the gradient covariance matrix below a threshold as the weak textured patches. The noise level $\hat{\sigma}_n^2$ is estimated from the

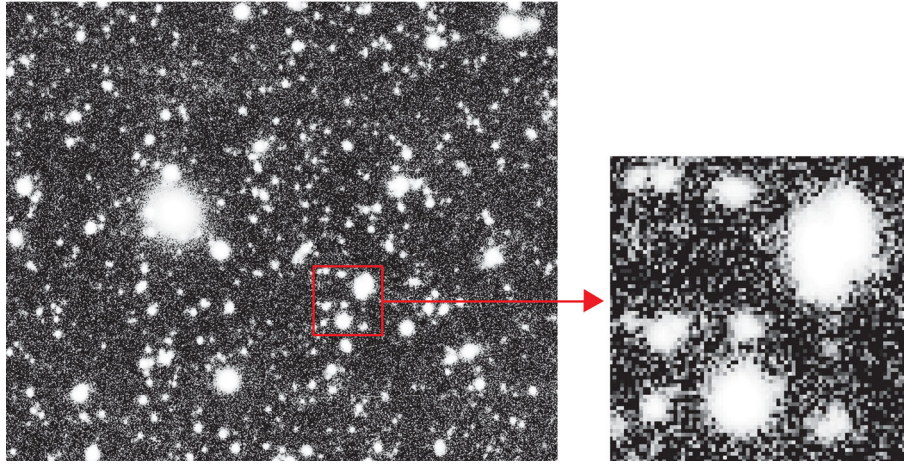


Figure 6. The result of histogram equalization. The right image shows an enlarged view of the sub-region in the rectangle. Histogram equalization results in enhanced contrast of objects, background, and clearer object boundaries.

selected weak textured patches based on the theory of PCA. After mathematical deductions, $\hat{\sigma}_n^2$ can be simply estimated as

$$\hat{\sigma}_n^2 = \lambda_{\min} \left(\sum_{y'} \right), \quad (4)$$

where $\sum_{y'}$ denotes the covariance matrix of the selected weak textured patches and $\lambda_{\min} \left(\sum_{y'} \right)$ represents the minimum eigenvalue of the matrix $\sum_{y'}$.

Once the noise level has been calculated, the window size of Gaussian filter is modified dynamically and adapted according to the following criterion: if the noise level is high, the size of the window will be increased, otherwise, the size of the window should be decreased.

Note that this adaptive noise removal procedure is so far only used in the local method pipeline. The computation was prohibitively time-consuming in our implementation when applied to a full resolution astronomical image. The noise-level estimation iteratively selects weak textured patches (7×7) and computes the noise level $\hat{\sigma}_n^2$ until $\hat{\sigma}_n^2$ is unchanged. When applying this technique to a large full resolution data set, the image will be divided into many small patches needed for the iterative computation and selection of weak textured patches, creating very long processing times.

For the global method, a fixed-sized Gaussian filter window is used instead to give a preliminary set of results. Given sufficient computing resources and optimized code, a global adaptive Gaussian filter might yield even better results.

2.3.4 Layered object detection

Due to the large dynamic intensity range and the large ratio between the area of the smallest and the largest objects presented in an astronomical image, detecting faint objects is difficult. In order to detect more faint objects, especially those in the neighbourhoods of bright ones, a layered object detection scheme is applied based on Otsu's method (Otsu 1979).

Objects are detected by classifying pixels that belong to objects and separated from the background according to a threshold. In his paper, Otsu uses an algorithm to search for an optimum threshold t_{op} , which minimizes the intra-class variance σ_ω^2 (a weighted sum of the variance within objects and that within the background), to

distinguish objects and the background. The intra-class variance σ_ω^2 is computed as

$$\sigma_\omega^2(t) = \omega_1(t) \sigma_1^2(t) + \omega_2(t) \sigma_2^2(t), \quad t = 1, 2, \dots, I_{\max}, \quad (5)$$

$$\omega_1 = \sum_0^t p(i), \quad (6)$$

$$\omega_2 = \sum_{t+1}^{I_{\max}} p(i), \quad (7)$$

where t represents all the candidate thresholds, I_{\max} is the maximum intensity of the image, $p(i)$ is the value of the i th bin in the intensity histogram of the image, ω_1 and ω_2 stand for the probabilities (weights) of objects and the background classified by the threshold t , and σ_1^2 and σ_2^2 are the variances of objects and the background, respectively.

Using the threshold t_{op} , the image is converted into a binary image where the pixels are mapped to 1 (where the original pixel intensities below the threshold) or 0 (where the original pixel intensities above the threshold). The pixels with value 0 are preliminary detected objects.

Because of the high intensity of the brightest objects in each sub-region, the initial detection threshold computed may not be appropriate. This limiting factor is also mentioned by `SEXTRACTOR`, which uses a simple median filter to suppress possible background overestimations due to bright stars in each of their 32×32 image tiles. Although median filter can be applied to improve the estimation of the background for increasing the accuracy of the calculated detection threshold, we found that relatively bright objects will still cause fainter objects to be discarded with the background. To improve this, we propose a layered detection scheme to detect fainter objects in the neighbourhood of brighter ones.

As mentioned in Section 2.3.1, each sub-region divided by the watershed segmentation method includes at least one bright object. These bright objects can weaken the detection capabilities of fainter objects. To reduce this adverse influence, we apply a layered detection scheme in each sub-region partitioned as follows.

(I) Detect objects by Otsu's method and only keep the large and bright ones.

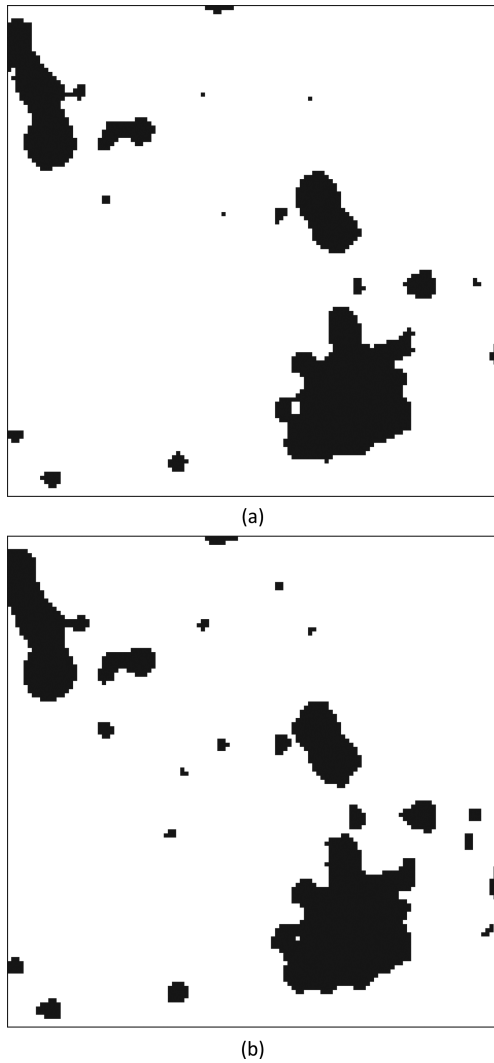


Figure 7. Results of the layered object detection approach. Panel (a) shows the detection results of directly using Otsu's method to detect all objects, and panel (b) shows the result obtained when adapting the layered detection strategy to extract faint objects and bright objects separately. Comparing panels (a) and (b), more faint objects can be detected by the layered detection step.

(II) Subtract the detected large and bright objects from the transformed image (the image obtained after background subtraction), and mark the residual image as image *A*.

(III) Set the intensity of the body area of the subtracted large and bright objects to the mean intensity of image *A*. This generates a new residual image *B*.

(IV) Apply histogram equalization, adaptive Gaussian filter and Otsu's method again to image *B* to detect more faint objects. The median filter is used in the detection results (the binary image obtained) to remove very small objects as outliers.

(V) Combine the bright objects retained by step (I) and all small and faint objects detected by step (IV) as the final detection result.

Fig. 7 demonstrates the results of the layered object detection. Compared to Fig. 7(a), Fig. 7(b) clearly shows that more faint objects are detected by this layered approach.

2.3.5 Deblending

When applying the layered object detection routine described in the previous section, it is possible that a group of adjacent pixels are detected as a single object or overlapping 'blended' objects. Deblending is a separation scheme that decides whether a set of pixels (a preliminary detected object) should be separated into additional objects. Here we apply the multi-threshold method which is similar to the approach used in *SEXTRACTOR*. This method first defines N thresholds exponentially spaced between the minimum and the maximum intensity of the preliminary detected object in the following form:

$$T_i = I_{\min} \cdot (I_{\max}/I_{\min})^{(i/N)}, \quad i = 1, 2, \dots, N, \quad (8)$$

where I_{\min} and I_{\max} are the minimum and maximum intensity of the preliminary detected object, respectively, and N is the number of the defined thresholds.

A tree structure is constructed by branching every time when pixels above a threshold T_i can be separated from pixels below it. A branch is considered as a separate object when at a branch level i of the tree, there are at least two branches which satisfy the following condition: the sum of intensity of each branch is larger than a certain fraction p of the total intensity of the tree. The N and p parameters are set to 32 and 0.001, respectively, in our experiment.

The outlying pixels which have a flux lower than the separation thresholds T_i need to be assigned to their own proper objects. We adapt the watershed segmentation method described in Section 2.3.1 to perform this separation. The objects identified by the multi-threshold method are used as the seed points and, in the process, consider the outlying pixels as objects that need to be merged with the seed points. To complete the deblending process, the outlying pixels are finally merged into their respective neighbouring objects. Fig. 8 shows the results of a successful deblending operation.

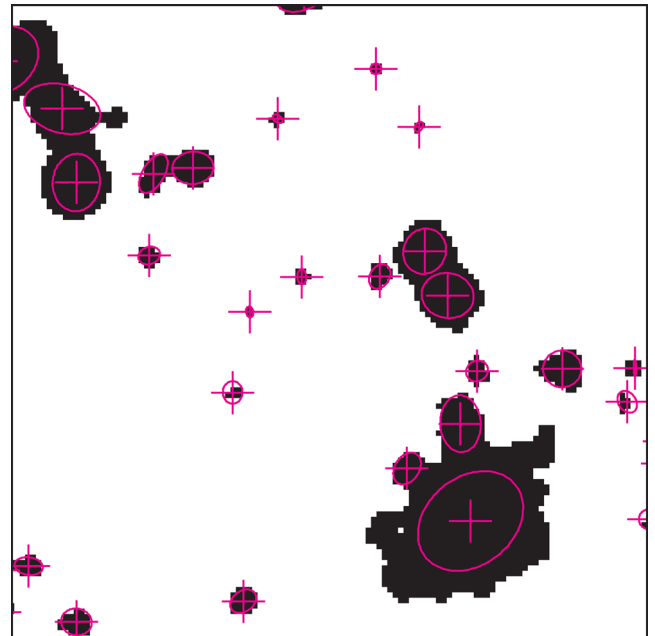


Figure 8. The result of the deblending operation. Each group of black connected pixels is considered as one preliminary detected object. Deblending is used to check these objects and separate them as separately objects. A real single object obtained by the deblending step is marked by an ellipse, and plus signs represent the centre of objects.

3 TESTS AND RESULTS

3.1 Data sets

Simulated astronomical data made public by the Large Synoptic Survey Telescope (LSST) image simulation group and a sample of observational data from the Deep Lens Survey (DLS; Wittman et al. 2002) are used to evaluate the accuracy of our approach.

3.1.1 LSST data set

The LSST ImSim data set² (Connolly et al. 2010) is a high-fidelity simulation of the sky. CCD images of size 4096×4096 pixels are generated by simulating a large-aperture, wide-field survey telescope and formatted as Flexible Image Transport System (FITS) files. These images simulate the same sky field but with varying airmass, seeing, and background. The ground-truth catalogues of these synthetic images are also offered which are used to test and evaluate the algorithm presented in this paper.

For the following benchmarks, the synthetic images ‘Deep_32.fits’ and ‘Deep_36.fits’ are selected to show the detection results of our method and a competing method. Both of the images contain the same airmass and sky background model but differ in noise levels and seeing.

According to the catalogue provided by the LSST group, there are 199 356 galaxies and 510 stars present in each LSST simulation. Due to the large number of simulated galaxies and variables, most of the galaxies are too faint in image space and overlap one another, resulting in many barely visible or non-visible and hard-to-detect objects. Therefore, before using these catalogues as the ground truth, invisible galaxies are discarded by the following criteria: if the magnitude (r_mag in the LSST catalogue) of a galaxy is smaller than r_mag_t , it will be kept as a visible object; otherwise, it will be discarded. r_mag_t is computed as follows:

$$r_mag_t = r_mag_{\min} + (r_mag_{\max} - r_mag_{\min}) \cdot T, \quad (9)$$

where r_mag_{\min} and r_mag_{\max} are the minimum and maximum magnitudes of galaxies in the LSST catalogue, and T is set to 0.35, which is a good value for keeping all objects that have the same brightness as the objects that can be detected by our method and S_{EXTRACTOR}.

By removing non-visible objects, this pre-processing step allows for accurate confirmation of detected objects with the ground-truth catalogue. Hereafter, these processed ground-truth catalogues will simply referred to as the ground truth.

3.1.2 DLS data set

The DLS data set³ used for testing is taken from a deep *BVRz* imaging survey that covers 20 sq. deg. to a depth of approximately 28th magnitude (AB) in *BVR* and 24.5 in *z*(AB). Our subsample includes four FITS files of size 2001×2001 . The survey was taken by the National Optical Astronomy Observatory’s (NOAO) Blanco and Mayall 4 m telescopes. The images ‘R.fits,’ ‘V.fits,’ ‘B.fits,’ and ‘z.fits’ in the DLS data set are observations of the same sky area using four different waveband filters, chosen so as to include a representative sample of objects and imaging artefacts.

² <http://lsst.astro.washington.edu/data/deep/>

³ <http://dls.physics.ucdavis.edu>

Table 1. Detection results for the LSST data set.

	Total detected objects		True positives		Precision rate (%)	
	OM	SE	OM	SE	OM	SE
Image:						
Deep_32.fits	1433	1441	1310	1189	91.42	82.51
Deep_36.fits	1375	1386	1251	1138	90.98	82.11

Note. OM = our method; SE = S_{EXTRACTOR}.

Since we lack a ground-truth catalogue, we compare the objects detected in different bands to gather a coinciding subset of detected objects which are likely to be real. Based on these cross-band identifications, we can reasonably estimate which objects are true positives and false positives. Since the *R* band is used as a detection band by the DLS survey due to its excellent depth and seeing, we verify the detection results of other bands by checking against the objects detected in the *R* band. In addition, we construct a ground-truth subset based on objects detected by both our method and S_{EXTRACTOR}.

3.1.3 Raw DLS data set

In order to test our software on a more difficult real-world data set, we selected a section from one of the individual unstacked DLS *R*-band input images. This image had been flat-fielded and sky-subtracted using the generic calibration data for DLS, otherwise no additional processing had been done; this image is called as ‘DLS_R_raw.fits’. An additional test image was generated by applying Malte Tewes’ PYTHON implementation⁴ of Van Dokkum’s L.A. Cosmic algorithm (Van Dokkum 2001) to remove obvious cosmic rays from the image. This implementation is a simple Laplacian filter to remove unrealistically pointy sources. The generated image is referred to as ‘DLS_R_cosmic_ray_cleaned.fits’. For both of these images, although we lack a ‘ground-truth’ image, we can refer to the equivalent stack of 20 DLS images at that sky location to learn which detections should be considered real and which spurious.

3.2 Evaluation on simulated data

The first experiment is designed to test our global detection pipeline on the LSST data set. We compare the accuracy of our method to S_{EXTRACTOR} using minor changes to S_{EXTRACTOR}’s default parameters. The parameters ‘DETECT THRESH’ and ‘DETECT MINAREA’ of S_{EXTRACTOR} are set to 1.64 and 1, respectively, in order to obtain the best detection and a comparable total number of detected objects. When dealing with artefacts around large detected objects, S_{EXTRACTOR} uses a ‘cleaning step’ to remove them while we use ‘open’ and ‘close’ morphological image processing operators with radius 2 for each neighbourhood. After this removal, detection results are compared to the ground truth. The detection results for images ‘Deep_32.fits’ and ‘Deep_36.fits’ are shown in Table 1, comparing the total number of objects detected and the true positive detection rate.

Although we detect fewer total objects with our method, we are able to identify 121 (8.91 percent) more genuine objects in the image ‘Deep_32.fits’. Within the total 1375 objects detected by our method in the image ‘Deep_36.fits’, there are 113

⁴ http://obswww.unige.ch/~tewes/cosmics_dot_py/

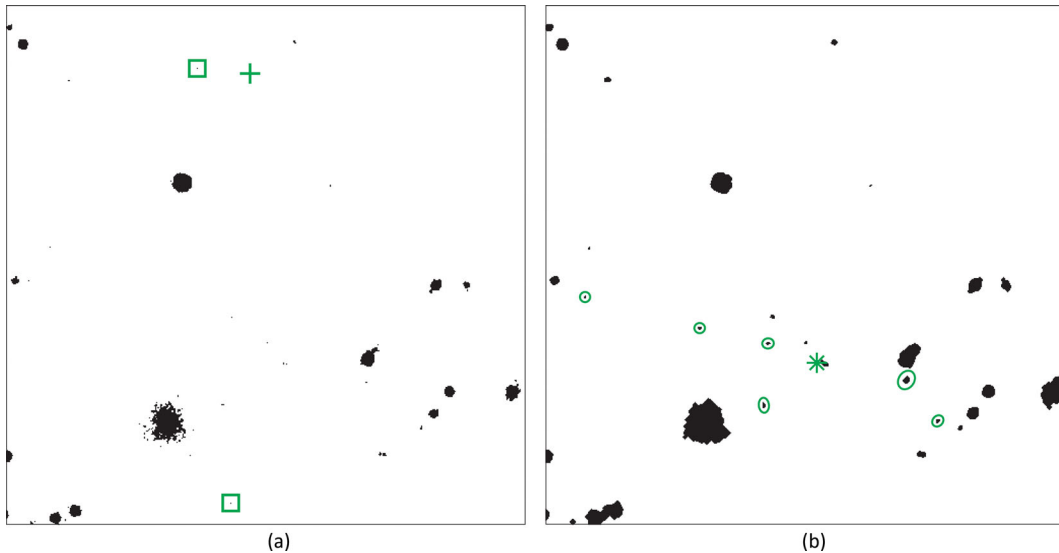


Figure 9. Unique objects detected by our method and SExtractor. Panel (a) shows the detection result of exclusive to SExtractor, where squares mark true positives and the plus signs mark false positives; panel (b) shows the exclusive detection results of our method, where ellipses mark real objects and the asterisk marks a false detection. The black pixel regions without any marks are the objects detected by both methods.

Table 2. Unique objects detected by our method and SExtractor.

	Image	
	Deep_32.fits	Deep_36.fits
Objects detected by OM and not by SE:		
True	228	219
False	112	108
Objects detected by SE and not by OM:		
True	107	106
False	225	216

Note. OM = our method; SE = SExtractor.

(8.87 per cent) more true positives compared to SExtractor. Our method also generates a smaller number of false positives.

We also compare the objects exclusively detected by each method. Unique objects detected by each method in a 512×512 -sized sub-region of ‘Deep_32.fits’ are shown in Fig. 9. The numerical detection results in the entire image are provided in Table 2.

Taking the unique detection results for the image ‘Deep_32.fits’ as an example, there are 340 objects (23.73 per cent of 1433 total detected objects) that can be detected only by our method, and 228 (67.06 per cent) objects among them are real objects. SExtractor uniquely detects 332 objects (23.04 per cent of 1441 total detected objects) of which 107 (32.23 per cent) are real objects. Our method’s unique detections are more than twice as likely to be real objects compared to those only found by SExtractor.

Faint object detection is challenging and it is an important ‘cost and value factor’ in terms of optimal use of telescope time and higher density of objects. This makes a method that can detect more faint objects valuable and attractive. The standard astronomical magnitude ‘ R_{mag} ’ characterizes the brightness (large ‘ R_{mag} ’ values defining fainter objects). It is computed as

$$R_{\text{mag}} = \text{zero} - \text{point} - 2.5 \cdot \log_{10}(\text{TS}), \quad (10)$$

where ‘zero-point’ is the magnitude of an object that has only one count and TS is the total data counts of star.

To evaluate the ability of detecting faint objects, a log-histogram is used. This histogram does not represent the number of detected

objects with certain magnitude in each bin, but rather the logarithm of that number. The log-histograms of objects detected in the image ‘Deep_32.fits’ by our method and SExtractor are plotted in Fig. 10.

Fig. 10 shows that the distribution of the log-histogram of our method is wider than that of SExtractor (right side). The value of largest magnitude of objects detected by our method is about 28, while for SExtractor the largest magnitude is about 26. Fig. 10(a) justifies our discarding of objects that are too faint to be possibly detected in the ground truth and shows that the magnitudes of all visible objects retained are visible by our method and SExtractor.

To further evaluate the accuracy of our method, object position and angle are compared using the following two criteria:

(I) position difference, calculated as the Euclidean distance of the detected objects’ centre and the centre of the same objects in the ground truth, and

(II) position angle (the angle between the major axis of objects and the x image axis) difference, computed as the absolute difference between the position angle of detected objects and the true position angle of the same objects in the ground truth.

The average position difference of objects detected in the image ‘Deep_32.fit’ by our method is 0.6921 pixels, and the average position angle difference is 0.6054 rad; the average position difference of objects detected by SExtractor is 0.7128 pixels, and the average position angle difference is 0.7009 rad. Our method has, on average, a more accurate centre-point location detection than SExtractor. These results are plotted in Fig. 11 for position accuracy and Fig. 12 for angular accuracy.

Fig. 11 shows the position difference between detected objects and their ground-truth counterparts. Comparing the dashed curve and the solid curve, for objects with index smaller than 400 (i.e. large and bright objects), our method’s location accuracy is worse than SExtractor’s. This is most likely due to our finding the nearest pixel to the centre rather than interpolating to a fractional pixel location. However, for objects with an index larger than 400 (i.e. relatively small and faint objects), our method performs better than SExtractor. This may indicate that we have an advantage for centroiding small and faint objects. Comparing the left and right plots

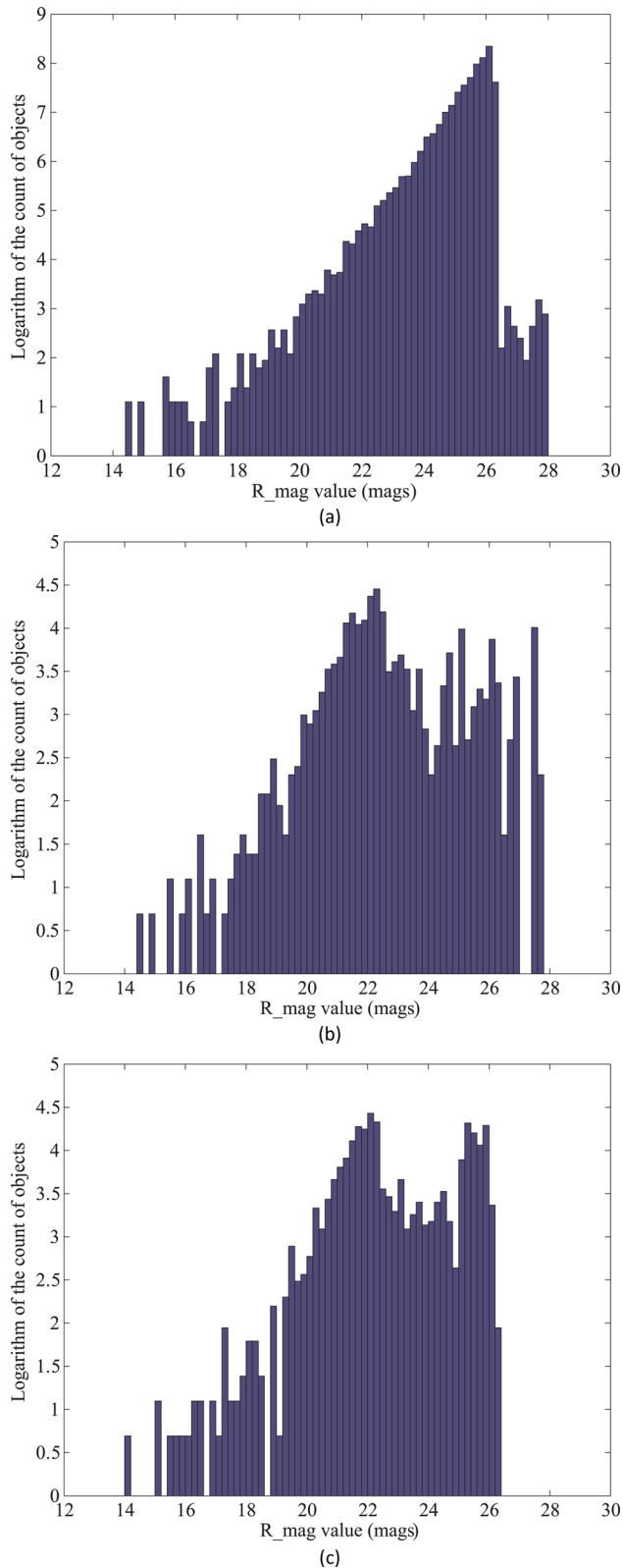


Figure 10. Log-histograms of detected objects. Panel (a) shows the log-histogram of the ground truth, panel (b) our method, and panel (c) SE_{EXTRACTOR}. The horizontal axis represents the value of magnitude, and the vertical axis represents the logarithm of the number of objects with that magnitude.

in Fig. 12, the position angle difference (delta-PA) of objects found by our method is generally smaller than SE_{EXTRACTOR}'s, especially for small objects. This becomes apparent when comparing the circle symbol objects, where our method is denser than SE_{EXTRACTOR} in the range of delta-PA less than 0.4. This demonstrates that our method is more accurate when describing the angular direction of objects.

To summarize, our method can detect more real and faint objects than SE_{EXTRACTOR} (Table 1 and Fig. 10), and, on average, has better location accuracy (shown in Figs 11 and 12). One limitation of our method is location accuracy of large and bright objects compared to SE_{EXTRACTOR}'s. Since SE_{EXTRACTOR} can detect more additional objects that we cannot detect (Fig. 9 and Table 2), SE_{EXTRACTOR} and our method can also be combined to detect objects more accurately and obtain more real and faint objects, overall.

3.3 Applying our local method to observational data

In order to show the adaptability of our method, we test it on real observational data. Due to lack of the ground truth, our detection results in *B*, *V*, and *z* are compared to results in the detection *R* band. Although this will bias our sample against objects with extreme colours (and also variable sources), when we compare our results to SE_{EXTRACTOR}'s results on the same data, the biases should be comparable.

Our global method is first used to extract objects where the 30 brightest objects are selected as seed points to generate sub-regions. Finally, our layered detection is carried out to detect objects. The parameters 'DETECT THRESH' and 'DETECT MINAREA' of SE_{EXTRACTOR} are set to 1.5 and 1, respectively, to detect a comparable total number of objects. Fig. 13 shows the detection results of our method and SE_{EXTRACTOR} for a 250×250 sub-region of the image 'V.fits'. It can be seen that most of the objects detected exclusively by our method are faint objects located near bright objects. Table 3 shows a quantitative comparison of the detection results.

Table 3 compares results for the different band images. Although the *R*-band objects detected by our method are about 60 fewer than the objects extracted by SE_{EXTRACTOR}, we can detect more objects in the *V*-, *B*-, and *z*-band images where objects are generally fainter. When comparing the objects detected in *V*-, *B*-, and *z*-band images to those in the *R* band, our method detects 85.25, 81.71, and 76.66 per cent true positive objects, while SE_{EXTRACTOR} detects 82.08, 83.8, and 74.27 per cent objects. Our method detects more objects in *V*- and *z*-band images with a higher percentage of objects which can be detected in the *R*-band image. Though the percentage of the *R*-band matched objects in the *B*-band image is smaller (about 2 per cent) than that of SE_{EXTRACTOR}, the total number of the matched objects (3524) is larger than that of SE_{EXTRACTOR} (2917). Overall, our method detects more objects in *V*-, *B*-, and *z*-band images where more faint objects are present. To obtain results with fewer false positives, a user could use SE_{EXTRACTOR} to extract objects in the image 'B.fits' and combine the results produced by both methods.

The distributions of the log-histograms of objects detected by our method and SE_{EXTRACTOR} for 'V.fits' are compared in Figs 14(a) and (b). This figure shows that the largest R_{mag} value (using instrumental magnitudes, with no zero-point applied) for objects detected with our method is about -2 , while the largest magnitude for objects found by SE_{EXTRACTOR} is about -3 . Although there are a few false positives in these results, this demonstrates that our method can detect fainter objects than SE_{EXTRACTOR}.

Due to the DLS data set not having a ground truth, we constructed a ground truth to compare both methods.

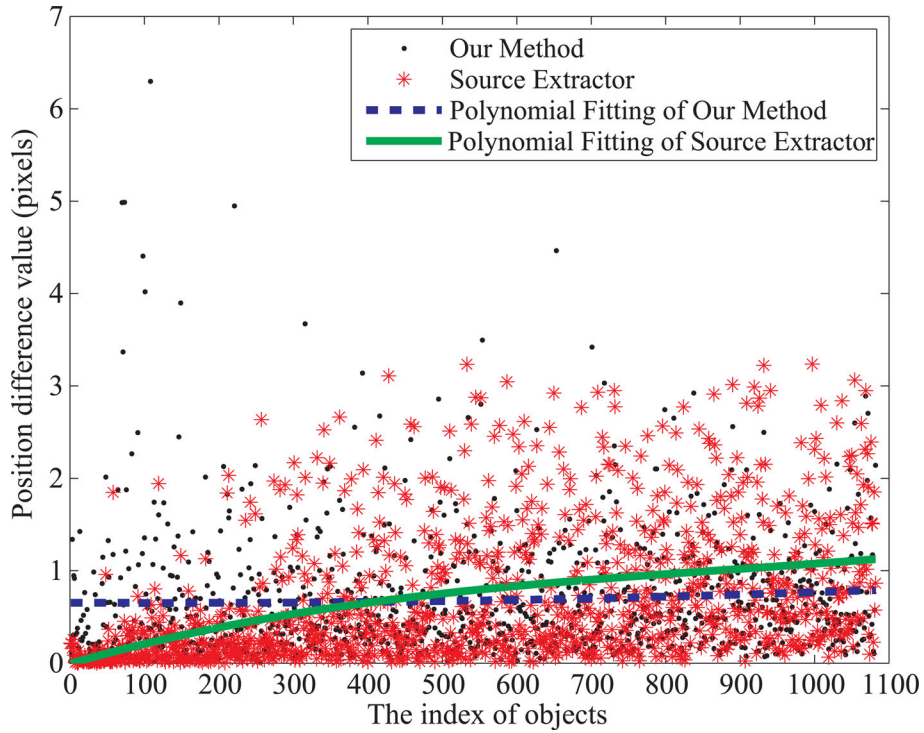


Figure 11. Position difference of our method and SE_{EXTRACTOR}. The horizontal axis represents the index of real objects detected by our method and SE_{EXTRACTOR}. (The smaller the index is, the larger and brighter the object is.) The vertical axis represents the value of the position difference. Dots indicate the position difference of our method, and the star symbols indicate the position difference of SE_{EXTRACTOR}. The dashed curve and the solid curve result when fitting the position difference of our method and SE_{EXTRACTOR} by a third-order least-squares polynomial, respectively.

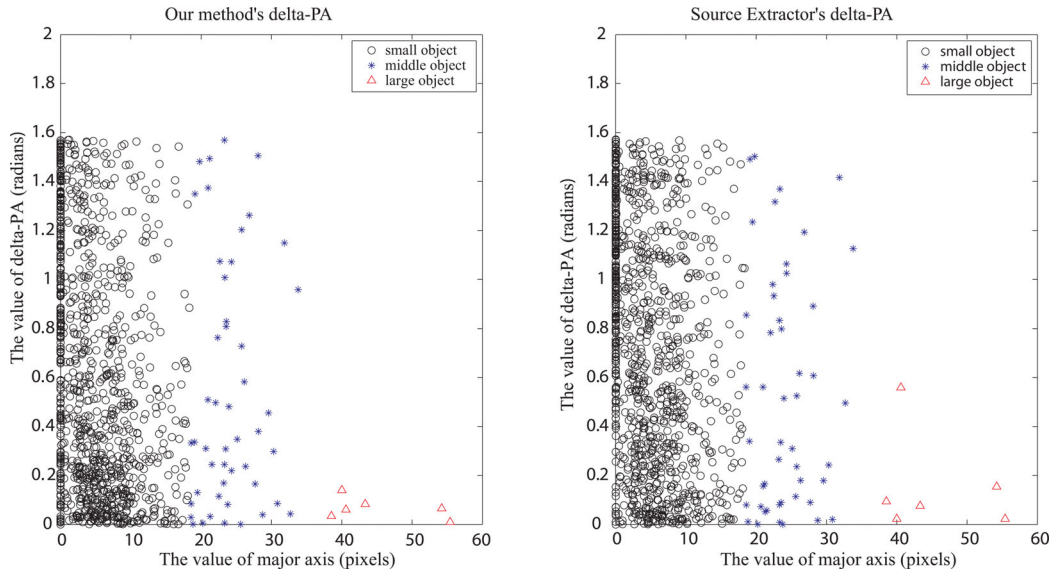


Figure 12. Angle difference of our method and SE_{EXTRACTOR}'s. The horizontal axis represents the size of the major axis of real objects detected by our method and SE_{EXTRACTOR}. The vertical axis represents the value of the position angle difference (delta-PA). Circle, star, and triangle symbols indicate the small-, middle-, and large-sized objects, separately. Our method captures 43.04 per cent of objects with $2 < \text{major axis} < 10$ correct to within 15 deg, while SE_{EXTRACTOR} only achieves 28.75 per cent.

The ground truth of the DLS data set is constructed as follows:

- (I) compute the intersection of objects detected in the different band images by our method and call this intersection Inter_{our},
- (II) compute the intersection of objects detected by SE_{EXTRACTOR} in the different band images and call this intersection Inter_{SE}, and

(III) calculate the union of Inter_{our} and Inter_{SE} and view it as the ground truth of the DLS data set.

Since the z -band image is a lossy image, we construct two different ground truth of data set. One is constructed by computing the intersection of the objects detected in all band images in the DLS

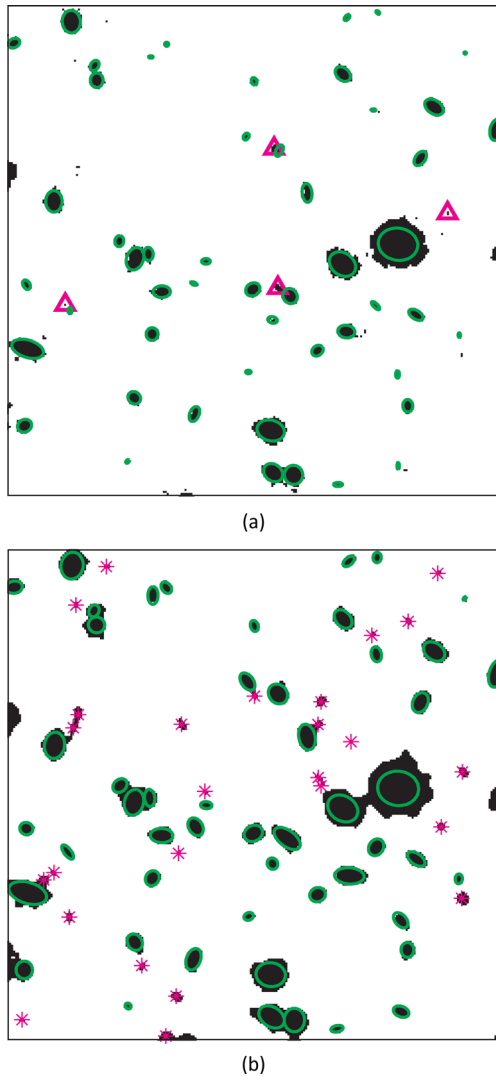


Figure 13. Detection results obtained with SExtractor (a) and our method (b). Ellipses in panels (a) and (b) represent objects that can be detected by both methods, triangles in panel (a) represent the objects detected exclusively by SExtractor, while the star signs in panel (b) represent the objects detected uniquely by our method.

Table 3. Detection results for the DLS data set.

	Total detected objects		Matched objects		Precision rate (%)	
	OM	SE	OM	SE	OM	SE
Image:						
V.fits	4421	4091	3769	3358	85.25	82.08
B.fits	4313	3481	3524	2917	81.71	83.80
z.fits	3115	2876	2388	2163	76.66	74.27

Note. OM = our method; SE = SExtractor. Matched objects are objects detected in the images ‘B.fits’, ‘V.fits’, and ‘z.fits’ that can also be detected in the image ‘R.fits’. Our method and SExtractor detect a total of 6065 and 6126 objects in the image ‘R.fits’, respectively.

data set, called GT_RVBZ; the other one is called GT_RVB and it does not consider the z band.

When the union is computed for both GT_RVBZ and GT_RVB, we first include the mutually exclusive objects detected by both our method and SExtractor. For objects found by both methods, we compute the averages of object descriptors (e.g., R_{mag} and

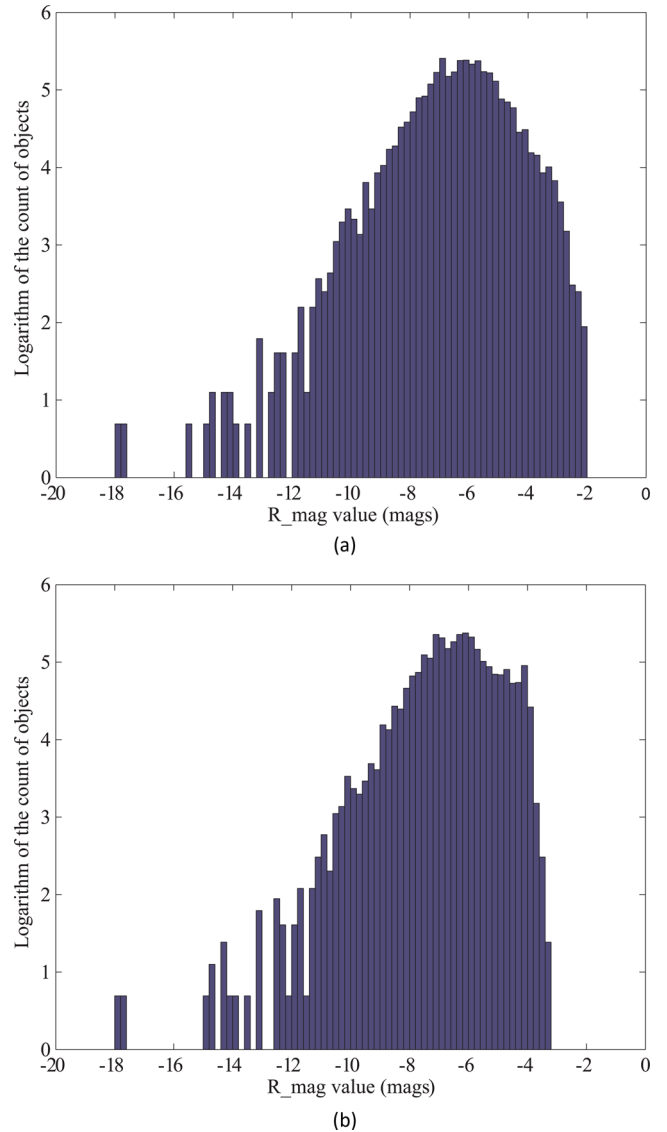


Figure 14. Log-histograms of objects detected in the image ‘V.fits’. Panels (a) and (b) show the log-histograms of our method and SExtractor, separately. The horizontal axis represents the value of magnitude and the vertical axis represents the logarithm of the number of objects with that magnitude.

position) and add them into the ground-truth catalogue. The results of comparing the two methods based on the constructed ground-truth catalogues are shown in Table 4.

Table 4 shows the numbers of true positives for the detection results of both methods. Our method can detect 82, 171, and 284 more real objects in the V -, B -, and z -band images compared to SExtractor when using the lossy GT_RBVZ as ground truth. When using GT_RBV as ground truth, our method detects 335, 413, and 212 more real objects compared to SExtractor. Our method has overall better detection capability concerning fainter and smaller objects. Regarding images where objects are brighter and larger, our method has detection capability comparable to that of SExtractor.

The tests performed for the observational data set demonstrate that our method is better suited for detecting fainter objects. Hence, our method can also be used as an additional tool to detect the faint objects that would be missed by SExtractor.

Table 4. The number of true positives.

	GT_RBVZ		GT_RBV	
	OM	SE	OM	SE
The average number of true positives in R.fits	2061	2070	3199	3212
The average number of true positives in V.fits	2053	1971	3197	2862
The average number of true positives in B.fits	2046	1882	3192	2784
The average number of true positives in z.fits	1991	1707	2003	1781

Note. OM = our method; SE = SE_{EXTRACTOR}.

3.4 Applying our local method to raw stacked DLS data set

To further evaluate our pipeline, we select a raw observational data set that contains a noise not present in the previous data sets.

In this data set, two unstacked DLS images are used as a detection benchmark and one $20 \times$ stacked DLS image named ‘DLS_R_stacked.fits’ as the ground truth. One of the unstacked images is an *R*-band image named ‘DLS_R_cosmic_ray_cleaned.fits’ from which we remove cosmic rays using edge detection. This data set provides a high-noise test case for DLS. The other unstacked image is the raw *R*-band image named ‘DLS_R_raw.fits’.

Detection is first applied to the ground-truth image, and then to the unstacked DLS images, and a comparison is performed. The detection results of our method are compared to the results of SE_{EXTRACTOR}. The parameters ‘DETECT THRESH’ and ‘DETECT MINAREA’ of SE_{EXTRACTOR} are set to 1.5 and 1, respectively, to detect a comparable total number of objects in the unstacked images. The same parameters are changed to 1.33 and 1, respectively, to detect a comparable total number of objects in stacked images by our method.

Fig. 15 shows the object detection results of our method and SE-1.33-1 for a 250×250 sub-region of the image ‘DLS_R_stacked.fits’. Unfortunately, we do not have ground-truth data, and we cannot confirm that our method can detect more objects than SE_{EXTRACTOR}; nevertheless, we can state that the objects exclusively detected by our method are faint objects. As mentioned above, combining the detection results of our method and SE_{EXTRACTOR} can increase the total number of detected faint objects.

Table 5 shows the detection results by both methods.

Considering Table 5, when comparing our method to SE-1.5-1, our method can detect 823 more objects than SE-1.5-1. Although both methods can detect similar numbers of objects in ‘DLS_R_raw.fits’ and ‘DLS_R_cosmic_ray_cleaned.fits’, our method is able to detect the largest percentage of true objects (50.25 per cent). When compared to SE-1.33-1, our method and SE-1.33-1 can detect almost the same objects (nearly 6300) in the image ‘DLS_R_stacked.fits’. Although SE-1.33-1 can detect more objects in the two unstacked images compared to SE-1.5-1, the results also include more false objects (about 2 per cent more false objects than resulting from our method). In summary, our method can detect more objects with less false objects compared to SE_{EXTRACTOR}.

The log-histogram distribution of objects detected by our method and that by SE-1.33-1 for ‘DLS_R_stacked.fits’ are shown in Figs 16 (a) and (b). It can be seen that the largest R_{mag} value for objects detected by our method is about -2 , while the largest magnitude for objects found by SE_{EXTRACTOR} is about -4 . This demonstrates that our method can detect fainter objects than SE-1.33-1, although our method and SE-1.33-1 detect almost the same number of brighter objects in ‘DLS_R_stacked.fits’.

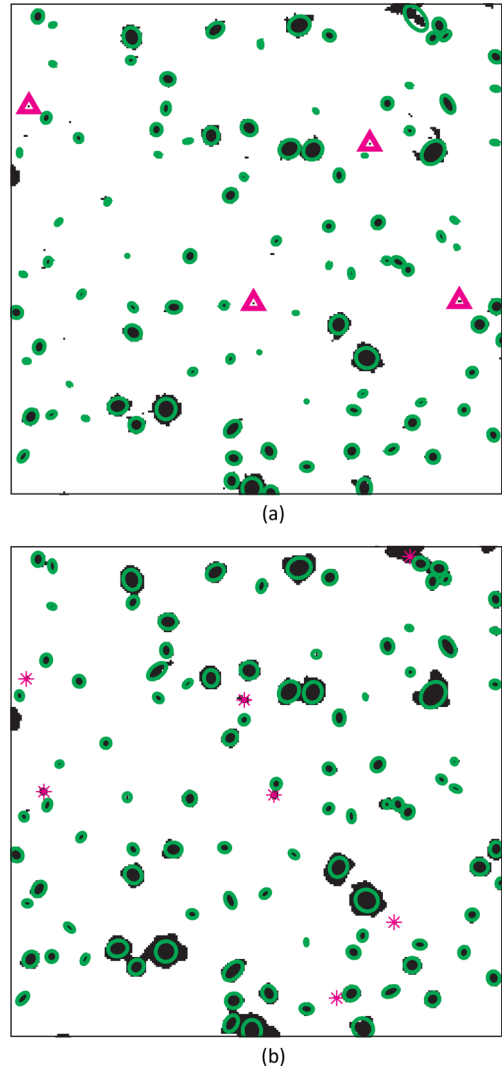


Figure 15. Detection results obtained with SE-1.33-1 (a) and our method (b). Ellipses in panels (a) and (b) represent objects that can be detected by both methods, triangles in panel (a) represent the objects detected exclusively by SE_{EXTRACTOR}, while the star signs in panel (b) represent the objects detected only by our method.

4 CONCLUSIONS

A novel approach for the detection of objects (stars and galaxies) in optical astronomical images has been proposed. Irregular sub-region division was constructed using the watershed segmentation algorithm. Adaptive noise removal strategy based on noise-level estimation and layered object detection step were effectively applied in each sub-region.

Table 5. Detection results for the raw stacked DLS data set.

Method:	DLS_R_stacked.fits		DLS_R_raw.fits		DLS_R_cosmic_ray_cleaned.fits		
	Total detected objects	Total detected objects	Matched objects	Precision rate (%)	Total detected objects	Matched objects	Precision rate (%)
OM	6381	2783	1392	50.02	2762	1388	50.25
SE-1.5-1	5558	2750	1294	47.05	2493	1226	49.18
SE-1.33-1	6387	3585	1698	47.36	3335	1629	48.85

Note. OM = our method; SE-1.5-1 = SExtractor using parameters ‘DETECT THRESH’ 1.5 and ‘DETECT MINAREA’ 1, SE-1.33-1 = SExtractor using parameters ‘DETECT THRESH’ 1.33 and ‘DETECT MINAREA’ 1. Matched objects are objects detected in the images ‘DLS_R_raw.fits’ and ‘DLS_R_cosmic_ray_cleaned.fits’ that can also be detected in the image ‘DLS_R_stacked.fits’.

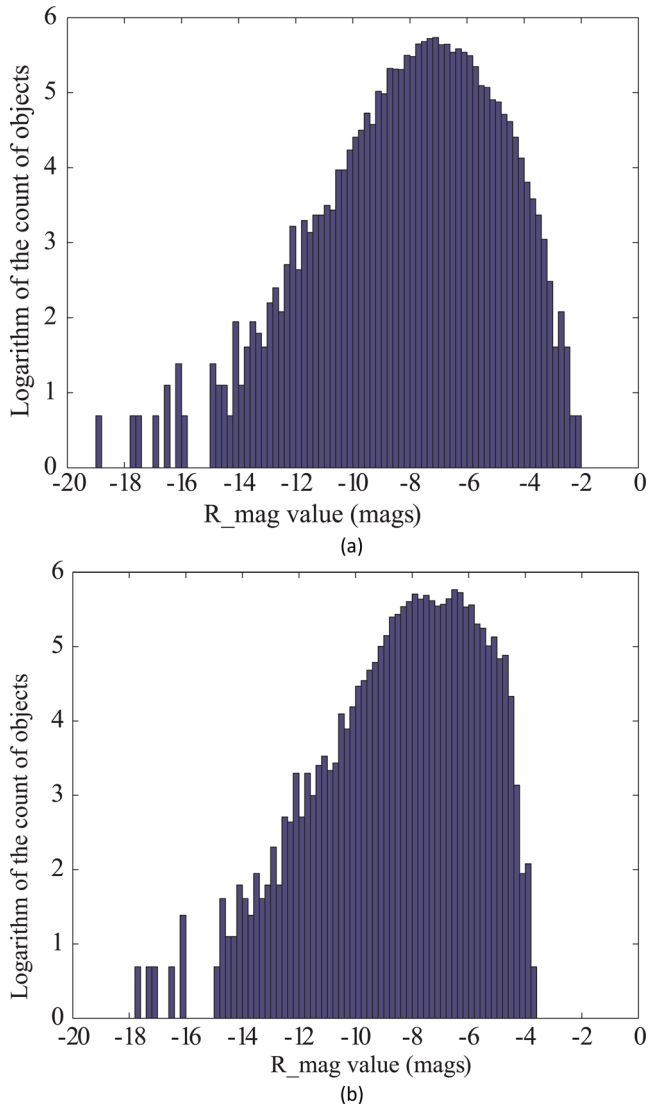


Figure 16. Log-histogram of magnitudes of objects detected in the image ‘DLS_R_stacked.fits’. Panel (a) shows the log-histogram of the magnitudes of objects detected by our method. Panel (b) shows the log-histogram of the magnitudes of objects detected by SE-1.33-1. The horizontal axis represents the magnitude and the vertical axis represents the logarithm of the number of objects having that magnitude.

We have compared results obtained with our software tool and with SExtractor. Specifically, our tool is particularly suited for detecting objects in regions that contain objects with low contrast relative to the background, or are very close to bright and large

object. Our tool can serve two purposes. It can be used as a stand-alone tool for processing astrophysical images or it can be used in combination with another tool, such as SExtractor, to increase the overall number of correctly recognized stars and galaxies. Considering the results discussed in this paper, it can be said that our method, when used in conjunction with a tool like SExtractor, identifies about 10 per cent additional true objects. Assuming a power-law distribution of faint object magnitudes with $\alpha = 0.6$ (uniform spatial distribution), our 10 per cent improvement in faint object density would be equivalent to 0.07 mag in additional survey depth, or approximately a 13 per cent decrease in the survey time required to reach a desired number density of galaxies per square arcminute. Assuming that these galaxies are not defective for some other reason (such as unreliable noise properties or shape bias), these expanded detection methods could measurably improve the speed and/or depth of large astronomical surveys such as LSST and PanSTARRS. A public version of our code has also been made available.⁵

In the future work, we will focus on improving the location accuracy of large object detection. We also plan on adding classification support for the detected objects.

ACKNOWLEDGEMENTS

We thank Masayuki Tanaka for making available his ‘NoiseLevel’ program. CZ acknowledges fellowship support from the China Scholarship Council (CSC). PT was partly supported by NSF grant AST-1108893.

REFERENCES

- Andreon S., Gargiulo G., Longo G., Tagliaferri R., Capuano N., 2000, MNRAS, 319, 70
- Bertin E., Arnouts S., 1996, A&AS, 117, 393
- Beucher S., Meyer F., 1993, in Dougherty E. R., ed., Mathematical Morphology in Image Processing, Vol. 34. Marcel-Dekker, New York, p. 433
- Blinchikoff H. J., Zverev A. I., 2001, Filtering in the Time and Frequency Domains. SciTech Publishing, Raleigh, NC
- Broos P. S., Townsley L. K., Feigelson E. D., Getman K. V., Bauer F. E., Garmire G. P., 2010, AJ, 714, 1582
- Connolly A. et al., 2010, The Large Synoptic Survey Telescope Image Simulation Group database
- Damiani F., Maggio A., Micela G., Sciortino S., 1997, AJ, 483, 350
- Gevrekci M., Gunturk B. K., 2009, Comput. Vis. Image Underst., 113, 565
- Guglielmetti F., Fischer R., Dose V., 2009, MNRAS, 396, 165

⁵ <https://github.com/zhengcx789/Object-Detection-in-Astronomical-Images>

- Laughlin S. B., 1981, *Z. Naturforsch.*, 36, 912
- Liu X., Tanaka M., Okutomi M., 2012, in Saber E., Hemami S., Sharma G., Rao R., Gurram P., eds, *Proc. 19th IEEE International Conference on Image Processing (ICIP)*, IEEE, Orlando, FL, p. 665
- Mangan A. P., Whitaker R. T., 1999, *IEEE Trans. Vis. Comput. Graphics*, 5, 308
- Masias M., Freixenet J., Lladó X., Peracaula M., 2012, *MNRAS*, 422, 1674
- Otsu N., 1979, *IEEE Trans. Syst. Man Cybern.*, 9, 62
- Peracaula M., Freixenet J., Lladó J., Martí J., Paredes J. M., 2009, in Bohlender D. A., Durand D., Dowler P., eds, *ASP Conf. Ser. Vol. 411, Astronomical Data Analysis Software and Systems XVIII*. Astron. Soc. Pac., San Francisco, p. 255
- Peracaula M., Lladó X., Freixenet J., Oliver A., Torrent A., Paredes J. M., Martí J., 2011, in Evans I. N., Accomazzi A., Mink D. J., Rots A. H., eds, *ASP Conf. Ser. Vol. 442, Astronomical Data Analysis Software and Systems XX*. Astron. Soc. Pac., San Francisco, p. 151
- Perret B., Lefevre S., Collet C., 2008, *Pattern Recognit*, 42, 470
- Slezak E., Bijaoui A., Mars G., 1988, *A&A*, 201, 9
- Stetson P. B., 1987, *PASP*, 99, 191
- Stil J. M. et al., 2006, *AJ*, 132, 1158
- Taylor A. R. et al., 2003, *AJ*, 125, 3145
- Torrent A., Peracaula M., Llado X., Freixenet J., Sánchez-Sutil J. R., Martí J., Paredes J. M., 2010, in Ercil A., Boyer K., Cetin M., Lee S., Unsalan C., eds, *Proc. 20th International Conference on Pattern Recognition (ICPR)*, IEEE, Istanbul, p. 4613
- Van Dokkum P. G., 2001, *PASP*, 113, 1420
- Wittman D. M. et al., 2002, *Proc. IEEE*, 4836, 73

This paper has been typeset from a $\text{\TeX}/\text{\LaTeX}$ file prepared by the author.